FULL PAPER

A New Strategy to Effectively Suppress the Initial Capacity Fading of Iron Oxides by Reacting with $LiBH_4$

Yun Cao, Yaxiong Yang, Zhuanghe Ren, Ni Jian, Mingxia Gao, Yongjun Wu, Min Zhu, Feng Pan, Yongfeng Liu, and Hongge Pan*

In this work, a new facile and scalable strategy to effectively suppress the initial capacity fading of iron oxides is demonstrated by reacting with lithium borohydride ($LiBH_4$) to form a B-containing nanocomposite. Multielement, multiphase B-containing iron oxide nanocomposites are successfully prepared by ball-milling Fe_2O_3 with $LiBH_4$, followed by a thermochemical reaction at 25–350 °C. The resulting products exhibit a remarkably superior electrochemical performance as anode materials for Li-ion batteries (LIBs), including a high reversible capacity, good rate capability, and long cycling durability. When cycling is conducted at 100 mA g^{-1}, the sample prepared from Fe_2O_3–0.2$LiBH_4$ delivers an initial discharge capacity of 1387 mAh g^{-1}. After 200 cycles, the reversible capacity remains at 1148 mAh g^{-1}, which is significantly higher than that of pristine Fe_2O_3 (525 mAh g^{-1}) and Fe_3O_4 (552 mAh g^{-1}). At 2000 mA g^{-1}, a reversible capacity as high as 660 mAh g^{-1} is obtained for the B-containing nanocomposite. The remarkably improved electrochemical lithium storage performance can mainly be attributed to the enhanced surface reactivity, increased Li^+ ion diffusivity, stabilized solid-electrolyte interphase (SEI) film, and depressed particle pulverization and fracture, as measured by a series of compositional, structural, and electrochemical techniques.

1. Introduction

With advantages of high energy density, long cycle life, and environmental benignity, lithium ion batteries (LIBs) are now the predominant power source for portable electronics and are considered the most promising power sources for electric vehicles and hybrid electric vehicles. Additionally, LIBs can be employed as energy storage and conversion devices from renewable resources such as solar and wind to buffer the intermittent and fluctuating supply of green energy and to smooth the difference between energy supply and demand.[1] The ever-increasing demand in various application areas generates great interest in searching for high-performance electrode materials with the ability to efficiently store and deliver more energy. Tremendous efforts have been devoted to searching for alternative anode materials with exceptional capacity, high energy density, and excellent cycling stability.[2] Among these materials, iron oxides have received much attention as anode materials for LIBs because of their high theoretical capacity, environmental benignity, cost efficiency, and natural abundance.[3] In particular, Fe_2O_3 can react with 6 Li^+ ions per formula unit through the following reaction, which delivers a theoretical capacity as high as 1007 mAh g^{-1}:[4]

$$Fe_2O_3 + 6Li^+ + 6e^- \leftrightarrow 3Li_2O + 2Fe \quad (1)$$

However, the use of iron oxides in LIB anodes also faces significant challenges due to the large volume change upon lithiation/delithiation and low electrical conductivity, which induces fast capacity fading, low Coulombic efficiency and poor rate capability.

Several strategies, including the fabrication of nanostructured materials and the use of composite carbonaceous materials, have been proposed to improve the durability and high rate capability of iron oxides.[5–18] The fabrication of nanostructured materials is relatively effective in accommodating the strain caused by the volume change upon lithiation/delithiation; these materials increase the electrode–electrolyte contact areas and shorten the lithium ion transport distance, therefore leading to good cycling stability and high rate capability.[5–12]

Y. Cao, Y. X. Yang, Z. H. Ren, N. Jian, Prof. M. X. Gao, Prof. Y. J. Wu, Prof. Y. F. Liu, Prof. H. G. Pan
State Key Laboratory of Silicon Materials
Key Laboratory of Advanced Materials and Applications for Batteries of Zhejiang Province
and School of Materials Science and Engineering
Zhejiang University
Hangzhou 310027, China
E-mail: mselyf@zju.edu.cn
Prof. M. Zhu
School of Materials Science and Engineering
Key Laboratory of Advanced Energy Storage Materials of Guangdong Province
South China University of Technology
Guangzhou 510640, China
Prof. F. Pan
School of Advanced Materials
Peking University
Shenzhen Graduate School
Shenzhen 518055, China
Prof. Y. F. Liu
Key Laboratory of Advanced Energy Materials Chemistry (Ministry of Education)
Nankai University
Tianjin 300071, China

DOI: 10.1002/adfm.201700342

Various nanostructured iron oxides have been synthesized and tested as anodes, including nanoparticles, nanowires, nanobelts, nanorods, nanotubes, nanosheets, nanoflakes, nanospheres, and nanoflowers.[7–12] Lin et al. reported that α-Fe_2O_3 nanorods retained a reversible capacity of 837 mAh g^{-1} at a current density of 503 mA g^{-1} after 100 cycles.[8] In addition, α-Fe_2O_3 nanotubes delivered a high capacity of 810 mAh g^{-1} at 1000 mA g^{-1} after 60 cycles.[9] Moreover, α-Fe_2O_3 nanosheets exhibited stable cycling performance with a reversible capacity of 518 mAh g^{-1} after 50 cycles in the potential range from 0.05 to 2.5 V at 0.1 C.[10] Porous Fe_2O_3 nanocubes showed a high specific capacity (800 mAh g^{-1} at 200 mA g^{-1}) and an excellent cycling stability with almost no additional capacity fading over the first 50 cycles.[11] The reversible capacity of hierarchical α-Fe_2O_3 hollow spheres with sheet-like subunits stabilized at 710 mAh g^{-1} after 100 cycles when cycling was conducted at 200 mA g^{-1} between 0.05 and 3 V.[12] Alternatively, the use of composite carbonaceous materials is another popular and effective approach to improve the electrochemical performance of iron oxides; these materials relieve the stress induced by volume change, increase electrical conductivity and alleviate pulverization and aggregation of the active materials.[13–18] Carbon-coated α-Fe_2O_3 hollow nanohorns grafted onto CNT backbones showed a stable capacity of 800 mAh g^{-1} for 100 cycles at 500 mA g^{-1}.[14] The anchoring of porous rod-shaped Fe_3O_4 particles on reduced graphene oxide led to a high reversible capacity, good rate capability and excellent stability.[15] The capacity was maintained at 890 mAh g^{-1} after 100 cycles at a current density of 500 mA g^{-1}. The hierarchical porous Fe_3O_4/VO_x/graphene nanowires delivered a reversible capacity of ≈500 mAh g^{-1} even at the high current density of 5 A g^{-1}.[16] Iron oxides supported on a flexible 3D CBC aerogel exhibited stable cycling performance of 950 mAh g^{-1} for 200 cycles at 800 mA g^{-1}.[17] The α-Fe_2O_3 nanorod arrays grown on reduced graphene oxide retained a high stable Li^+ storage capacity of 1200 mAh g^{-1} after 500 cycles at 0.2 C and an excellent rate capability of 775 mAh g^{-1} at 1.6 C.[18] Although the cycling stability and the rate capability of iron oxide-based anodes have been significantly improved by fabricating nanostructured materials and compositing with carbonaceous materials, these materials are generally synthesized under high temperature and high pressure using autoclaves, which is often time consuming and costly, thereby hampering the potential for economical large-scale production.

In this work, we proposed a new, facile and scalable strategy to improve the electrochemical lithium storage performance of iron oxides; in particular we sought to suppress the initial capacity fading by reacting with lithium borohydride ($LiBH_4$) to form B-containing nanocomposites. The B-containing iron oxide nanocomposites were prepared by ball milling the Fe_2O_3–$x$$LiBH_4$ mixtures at 300 rpm for 2 h and dynamically heating the mixtures to 350 °C at 2 °C min^{-1}. The composition, structure and electrochemical Li storage properties of the resultant products were systematically studied, and the mechanism for the significantly improved cycling durability was discussed. The B-containing iron oxide nanocomposites exhibited remarkably superior electrochemical properties as anode materials for LIBs, including high reversible capacity, good rate capability and long cycling durability.

2. Results and Discussion

2.1. Preparation and Characterization of B-Containing Iron Oxide Nanocomposites

The B-containing iron oxide nanocomposites were prepared by ball milling Fe_2O_3–$x$$LiBH_4$ mixtures and then heating the milled products, as shown schematically in **Figure 1**a. After ball milling, mass spectrometer (MS) analyses of the residual gas inside the milling jar exhibited a distinct H_2 signal for the $LiBH_4$-containing samples (Figure S1a, Supporting Information). The H_2 signal intensified as the amount of $LiBH_4$ in the Fe_2O_3–$x$$LiBH_4$ mixtures increased. These results indicate that

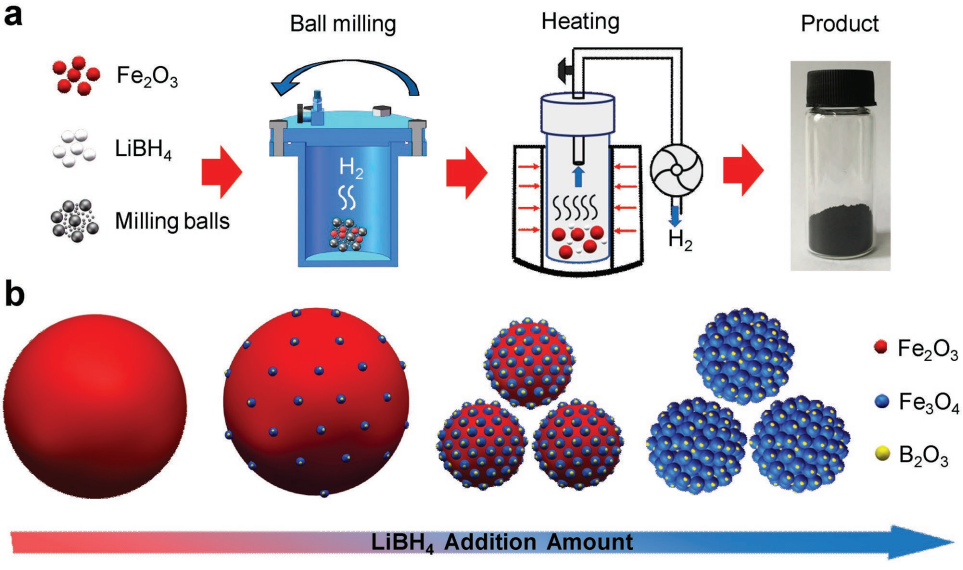

Figure 1. Schematic of the preparation process (a) and morphology (b) of B-containing iron oxide nanocomposites.

a chemical reaction occurred between Fe_2O_3 and $LiBH_4$ during ball milling of their mixtures because individual samples are relatively stable when they are ball milled separately. However, X-ray diffractometer (XRD) results (Figure S1b, Supporting Information) reveal that the characteristic reflections of α-Fe_2O_3 still dominate the XRD profiles of the B-containing samples, and no appreciable change is observed with increasing $LiBH_4$ content.

The milled samples underwent a dynamic heating process, and the MS and volumetric release curves were obtained as a function of temperature. As shown in **Figure 2**a, further hydrogen release was observed while heating samples from 25 to 350 °C. After heating to 350 °C, the resultant solid-state products were collected for structural and morphological characterization. Figure 2b shows the XRD patterns of the prepared B-containing samples. The results show that the sample prepared from Fe_2O_3–0.1$LiBH_4$ was mainly composed of α-Fe_2O_3. The characteristic reflections of Fe_3O_4 can also be observed at $2\theta = 30°$, 37°, 43°, and 57°, although their intensities are relatively weak. After increasing the $LiBH_4$ content in the starting mixtures, the reflections of Fe_3O_4 clearly intensified in the resultant samples, and those of α-Fe_2O_3 were weakened. When x in Fe_2O_3–$x$$LiBH_4$ was increased to 0.3, only the reflections of Fe_3O_4 were detected in the resultant samples; those of α-Fe_2O_3 disappeared completely. For the sample prepared from Fe_2O_3–0.4$LiBH_4$, the strongest reflection of metallic Fe at $2\theta = 45°$ could also be identified. These results indicate that during ball milling and subsequent heating, the reaction with $LiBH_4$ results in the gradual reduction of Fe_2O_3 to Fe_3O_4 or even metallic Fe because of the strong reduction process.[19,20] In addition, further careful examination revealed that two peaks at $2\theta = 42°$ and 62° were slightly asymmetric for the samples with higher $LiBH_4$ content, especially for the $x = 0.4$ sample, as two small shoulders were observed at the low-angle side. These two shoulders even developed into two distinct peaks when the $LiBH_4$ content was increased (Figure S1c, Supporting Information). Their position is located just near the two strongest reflections of $Li_2Fe_3O_5$. Moreover, it should be noted that the characteristic reflections of metallic Fe also gradually intensified with increasing $LiBH_4$ addition in the starting mixtures, as shown in Figure S1c (Supporting Information), suggesting increased relative content in the resultant products.

Further Fourier transform infrared (FTIR) examination (Figure 2c) provides additional evidence for the relative change in Fe_2O_3 and Fe_3O_4. It was observed that the characteristic absorption peaks of Fe_2O_3 at 563 and 476 cm^{-1} weakened and even disappeared; accordingly, the absorption peak of Fe_3O_4 emerged at 580 cm^{-1} and intensified as the $LiBH_4$ content in the starting mixtures increased.[21] Meanwhile, the absorbance of the B—O bond was also discernible at 1415 cm^{-1} in the B-containing samples,[22] and the intensity gradually increased with increasing the B content. This implies that the B element was possibly converted to the oxide in the resultant products. This conjecture was confirmed by analyzing the high-resolution X-ray photoelectron spectroscopy (XPS) spectra of B 1s. As shown in Figure 2d, a distinct peak for B 1s was observed at 192 eV in the B-containing samples; this peak can be attributed to B_2O_3, as previously reported.[23] The high-resolution XPS spectra of Fe 2p showed a gradual red shift in peak position with increasing B content (Figure 2e), providing additional evidence for a change from Fe_2O_3 to Fe_3O_4. Moreover, a weakening in the peak intensities of the Fe 2p XPS peaks was also observed, and can likely be attributed to the presence of B_2O_3 on the surface, as schematically indicated in Figure 1b.

According to the discussions above, it can be concluded that during ball milling and subsequent dynamic heating, Fe_2O_3 reacted with $LiBH_4$ and was gradually reduced to Fe_3O_4, $Li_2Fe_3O_5$, and even metallic Fe. This was accompanied by the

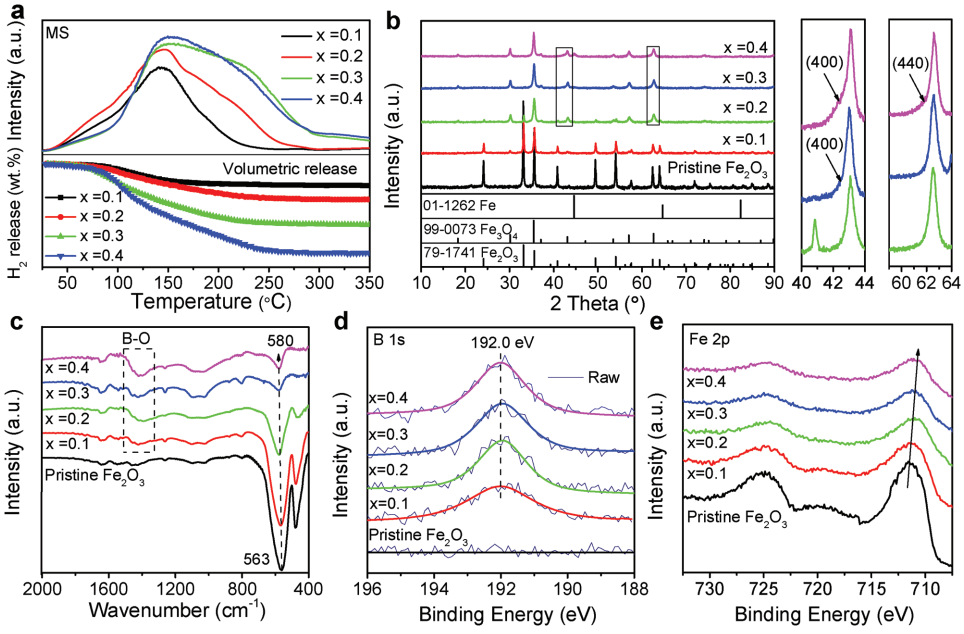

Figure 2. a) MS and volumetric release curves of ball-milled Fe_2O_3–$x$$LiBH_4$ samples. b) XRD patterns, c) FTIR spectra, and high-resolution XPS spectra of d) B 1s, e) Fe 2p of the prepared B-containing iron oxide nanocomposites.

release of hydrogen, and B_2O_3 was produced as described by the following reactions

$$12Fe_2O_3 + 2LiBH_4 \rightarrow 7Fe_3O_4 + Li_2Fe_3O_5 + B_2O_3 + 4H_2\uparrow \quad (2)$$

$$2Fe_3O_4 + 2LiBH_4 \rightarrow Li_2Fe_3O_5 + 3Fe + B_2O_3 + H_2\uparrow \quad (3)$$

Thus, after ball milling and heating of the mixtures of Fe_2O_3 and $LiBH_4$, the resultant product was mainly composed of Fe_2O_3, Fe_3O_4, $Li_2Fe_3O_5$, and B_2O_3, i.e., it is an oxide composite. Further Rietveld fitting results revealed the quantitative change in the relative phase content (Figure S2 and Table S1, Supporting Information), which matches well with the proposed reactions (2) and (3). It is clear that the relative content of Fe_2O_3 gradually decreased, and correspondingly, those of Fe_3O_4, $Li_2Fe_3O_5$, and B_2O_3 increased with increasing $LiBH_4$, due to the occurrence of reaction (2). In particular, Fe_3O_4 dominates the resultant $x = 0.3$ product along with the near disappearance of Fe_2O_3 and the formation of metallic Fe. More interestingly, the relative content of Fe_3O_4 slightly decreased for the $x = 0.4$ sample due to reaction (3). We therefore believe that reactions (2) and (3) reasonably describe the chemical reaction process of Fe_2O_3–$x$$LiBH_4$ mixtures during ball milling and dynamic heating.

Figure 3 displays the scanning electron microscope (SEM) and transmission electron microscope (TEM) images of the pristine Fe_2O_3 and B-containing samples. It is observed that the pristine Fe_2O_3 sample exhibited very irregular particle morphology and size, and a number of small particles aggregated into larger clusters (Figure 3a). In addition, some of the larger individual particles (>1 μm) had very smooth surfaces. For the B-containing samples, however, the particle size was relatively smaller, with a more uniform morphology, and the particle surface was clearly coarse. More interestingly, a large number of ≈10 nm nanoparticles were spread on the surface of the B-containing samples, and the nanoparticles grew distinctly in quantity with increasing B content (Figure 3b–e). A similar phenomenon was also observed in TEM images (Figure S3, Supporting Information). These nanoparticles dominate the $x >$ 0.1 samples and aggregate into the larger secondary particles (measuring ≈500 nm), as shown in Figure 3c–e. Further high-resolution transmission electron microscope (HRTEM) observation of the $x = 0.2$ sample indicated that the newly developed nanoparticles were mainly composed of Fe_3O_4, as the Fe_3O_4 (2 2 0) and (3 1 1) planes with interplanar spacings of 0.297 and 0.253 nm were identified in Figure 3f. Energy-dispersive X-ray spectrometer (EDS) mapping analyses confirmed the uniform distribution of elemental Fe and O (Figure S4, Supporting Information). It is well known that Fe_3O_4 offers better electric conductivity than Fe_2O_3.[24] The nanoparticles also make contact with the electrolyte and diffusion of lithium ions much easier. All these effects improve electrochemical Li storage performance. In addition, a thin amorphous layer was also observed on the surface of the nanoparticles and can be attributed to B_2O_3 in terms of FTIR and XPS results, as described above. Here, the amorphous form of B_2O_3 explains its nondetectability in the XRD profiles (Figure 2b). Thus, the resultant products by ball milling and dynamic heating the mixtures of Fe_2O_3-$x$$LiBH_4$ were identified as amorphous B_2O_3-containing iron oxide nanocomposites, which are described as B-containing iron oxide nanocomposites in this work.

2.2. Electrochemical Properties of B-containing Iron Oxide Nanocomposites

The prepared B-containing iron oxide nanocomposites were assembled into CR2025 coin-type cells, as active anode materials to evaluate their electrochemical Li storage performance. **Figure 4**a illustrates the first charge/discharge curves at a current density of 100 mA g^{-1}. All samples exhibited quite similar discharge/charge behaviors, as the majority of Li insertion occurs at ≈0.85 V and Li extraction occurs below 2.0 V, in good agreement with the Li storage process of nano-Fe_2O_3, as previously reported.[25] Encouragingly, the formation of

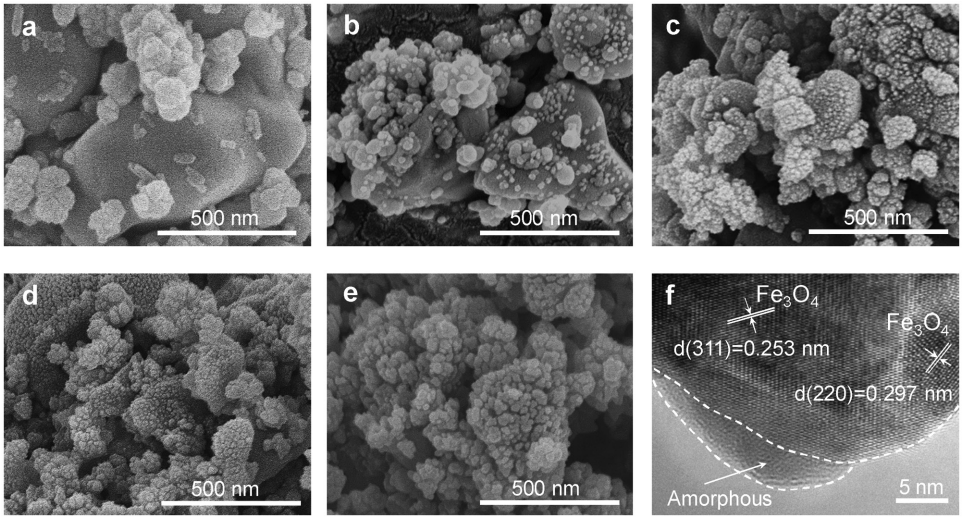

Figure 3. SEM images of a) pristine Fe_2O_3 and B-containing iron oxide nanocomposite samples for b) $x = 0.1$, c) $x = 0.2$, d) $x = 0.3$, and e) $x = 0.4$. f) High-resolution TEM image of the B-containing ($x = 0.2$) sample.

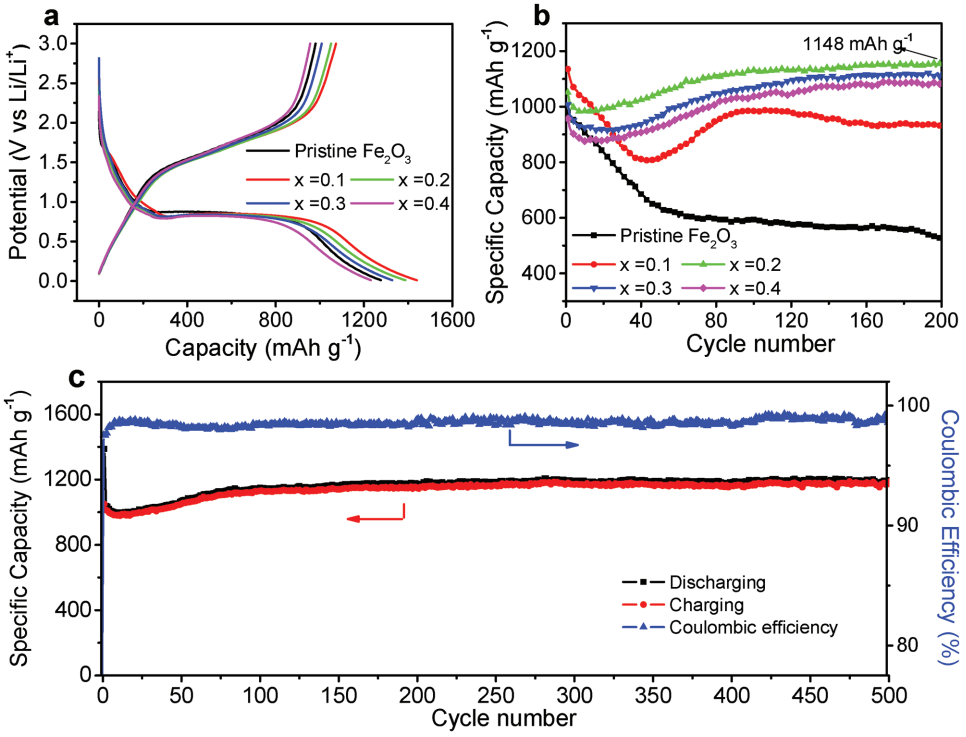

Figure 4. a) First charge/discharge curves and b) cycling performance curves of pristine Fe_2O_3 and prepared B-containing iron oxide nanocomposite samples at 100 mA g^{-1}. c) Specific capacity and coulombic efficiency of the B-containing ($x = 0.2$) sample after 500 cycles at 100 mA g^{-1}.

B-containing iron oxide nanocomposites improved the available capacity for electrochemical storage of Li in Fe_2O_3. The initial discharge/charge capacities of the samples prepared from Fe_2O_3–0.1$LiBH_4$, Fe_2O_3–0.2$LiBH_4$, and Fe_2O_3–0.3$LiBH_4$ were measured as 1439/1073, 1387/1051, and 1328/1009 mAh g^{-1}, respectively, at 100 mA g^{-1}, which are higher than those of the pristine Fe_2O_3 (1276/981 mAh g^{-1}). This can be ascribed to the increased utilization efficiency of active materials caused by the reduced particle and grain sizes, as observed in Figure 3. The corresponding initial Coulombic efficiency was determined to be approximately 74.6%, 75.9%, 77.2%, and 78.1% for the B-containing nanocomposites with $x = 0.1$, 0.2, 0.3, and 0.4, exhibiting a similar level to the pristine Fe_2O_3 (≈79.6%). Here, it is noteworthy that for B-containing nanocomposites, there is a slight but gradual reduction in initial discharge and charge capacities as the $LiBH_4$ content in the starting mixtures increases, whereas the Coulombic efficiency exhibits an opposite tendency. This should closely correlate with the sample component. As mentioned above, Fe_2O_3 reacted with $LiBH_4$ to convert into Fe_3O_4, $Li_2Fe_3O_5$ and even metallic Fe with the simultaneous generation of amorphous B_2O_3 during ball milling and subsequent dynamic heating. As a consequence, Fe_3O_4 is believed to be the primary active species for electrochemical Li storage in these B-containing nanocomposites. It is well known that the theoretical Li storage capacity of Fe_3O_4 (924 mAh g^{-1}) is lower than that of Fe_2O_3 (1007 mAh g^{-1}). Thus, the increased Fe_3O_4 content in the samples with increased $LiBH_4$ is responsible for the decreased specific capacities.

Figure 4b shows cycling performance curves for the pristine Fe_2O_3 and prepared B-containing nanocomposites over 200 cycles. As expectedly, the cycling stability of iron oxides was significantly improved with the formation of B-containing nanocomposites. During the discharging/charging process in the potential range of 0.01–3 V (vs Li/Li^+) at 100 mA g^{-1}, the capacity fading of the pristine Fe_2O_3 can be divided into two domains, as the specific capacity dramatically decreased from 981 to 610 mAh g^{-1} after the first 60 cycles and then sluggishly reduced to 525 mAh g^{-1} until 200 cycles. The capacity retention was calculated as 53%. For the B-containing nanocomposites, the capacity fading slowed significantly, especially within the first 60 cycles, and the sample prepared from Fe_2O_3–0.2$LiBH_4$ exhibited better overall electrochemical performance than the other samples taking into consideration the specific capacity and cycling stability. It was observed that the specific capacity of the sample prepared from Fe_2O_3–0.2$LiBH_4$ only decreased from 1051 to 980 mAh g^{-1} after the first 10 cycles. It then rose gradually and reached approximately 1148 mAh g^{-1} again at the 200th cycle, which is nearly twice the capacity of the pristine Fe_2O_3. Here, the capacity increase phenomenon is possibly ascribed to a pseudocapacitance effect caused by the interfacial Li storage mechanism, as previously reported.[26] After 500 cycles, the specific capacity still remained at 1176 mAh g^{-1} (Figure 4c), exhibiting excellent cycling stability.

The change in electrochemical Li storage behavior can be further understood by comparing the galvanostatic discharge/charge potential profiles of pristine Fe_2O_3 and $x = 0.2$ samples as a function of cycle. It is observed that at 10–500 cycles, the discharge/charge potential profiles of the B-containing nanocomposite remain nearly constant (**Figure 5**a). However, the pristine Fe_2O_3 sample exhibits a distinct shortening in the

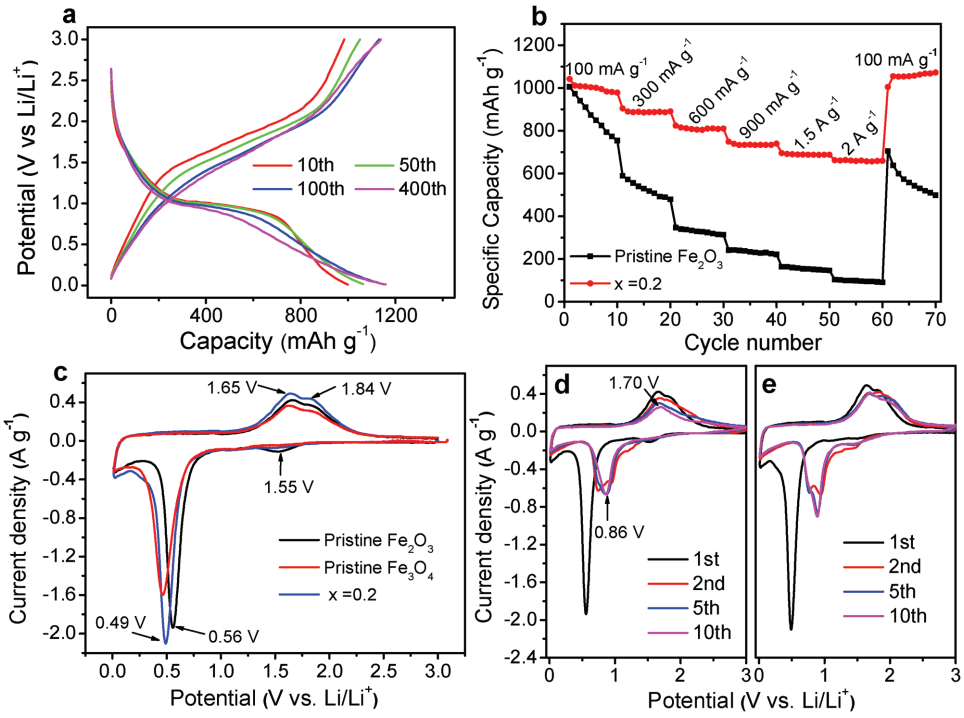

Figure 5. a) Charge/discharge curves at different cycles for the B-containing ($x = 0.2$) sample at 100 mA g^{-1}. b) Specific capacity of pristine Fe_2O_3 and B-containing ($x = 0.2$) samples obtained for cycles at different current densities. c) First CV curves of pristine Fe_2O_3, Fe_3O_4, and B-containing ($x = 0.2$) samples. d) CV curves of pristine Fe_2O_3 and e) B-containing ($x = 0.2$) samples.

potential plateaus and a gradual increase in the interval between the discharge and charge plateaus upon cycling (Figure S5a, Supporting Information), representing poor cycling stability and increased polarization, respectively. Moreover, comparison of the cycling durability of the samples prepared from Fe_2O_3–0.3$LiBH_4$ and Fe_2O_3–0.4$LiBH_4$ with pristine Fe_3O_4 was also conducted, as shown in Figure S5b (Supporting Information). These two samples mainly consist of the Fe_3O_4 phase. The results showed that the cycling durability of the samples prepared from Fe_2O_3–0.3$LiBH_4$ and Fe_2O_3–0.4$LiBH_4$ was also superior to that of the pristine Fe_3O_4, which further confirms that the formation of B-containing nanocomposites facilitates improved cycling stability of iron oxides. However, directly adding B_2O_3 did not significantly improve the cycling stability of either Fe_2O_3 or Fe_3O_4 (Figure S5c, Supporting Information), possibly due to the relatively loose contact and inhomogeneous distribution with respect to the in situ formed B_2O_3 from the redox reaction. In addition, the rate capability of iron oxides was also remarkably improved for the B_2O_3-containing iron oxide nanocomposites. As shown in Figure 5b, the specific capacity of the pristine Fe_2O_3 dropped rapidly as the current density increased and reached only 210 mAh g^{-1} at a current density of 2000 mA g^{-1} (≈2 C). The B-containing nanocomposite prepared from Fe_2O_3–0.2$LiBH_4$ delivered a reversible capacity as high as 660 mAh g^{-1} at the same rate, which is more than three times that of the pristine Fe_2O_3. This can be attributed to an enriched grain boundary and shortened diffusion distance caused by the multiphase structure and the reduced particle size, respectively, as described above.

Figure 5c–e compares the cyclic voltammetry (CV) curves of pristine Fe_2O_3 and the B-containing sample in the potential range of ≈0.01–3.0 V at a scan rate of 0.1 mV s^{-1}. As shown in Figure 5c, two peaks at ≈1.55 and 0.56 V were detected in the first cathodic process of the pristine Fe_2O_3. According to previous reports,[27] the weak peak at ≈1.55 V can be assigned to the process in which small quantities of lithium were inserted into Fe_2O_3 to form $Li_xFe_2O_3$, and the strong peak at ≈0.56 V corresponds to a reduction from Fe^{3+} and Fe^{2+} to Fe^0 and the irreversible reaction related to decomposition of the electrolyte. The anodic scan presented two adjacent peaks at ≈1.65 and 1.84 V that can be ascribed to the oxidation reactions of $Fe^0 \rightarrow Fe^{2+}$ and $Fe^{2+} \rightarrow Fe^{3+}$, respectively. For the B-containing nanocomposite, there is only one strong peak at 0.49 V in the first cathodic scan, and the weak peak at ≈1.55 V is not present, similar to the CV behavior of Fe_3O_4, which can be attributed to a reduction from Fe^{3+} to Fe^{2+}, as mentioned above. Compared with the pristine Fe_2O_3, the cathodic and anodic peaks of the B-containing nanocomposite were slightly intensified, representing an increase in the available storage capacities, as observed in Figure 4a. In the subsequent 2–10 cycles, the strong cathodic peaks of both the pristine sample and the B-containing nanocomposite shifted to a higher potential (≈0.86 V) with a decrease in peak intensities, as shown in Figure 5d,e; this is due to a large irreversible capacity loss. The two anodic peaks were gradually integrated into one peak at ≈1.70 V. In addition, it is noteworthy that there is a slight but continuous decrease in the intensities of the anodic peaks for the pristine Fe_2O_3 within 10 cycles, which indicates poor cycling stability. However, the CV curves of the B-containing nanocomposite are nearly stable and exhibit good reversibility after the 5th cycle. This result further confirms the significantly improved cycling durability

for the prepared B-containing nanocomposites along with the evaluation of the cycling performance (Figure 4c).

2.3. Mechanism for Improved Electrochemical Properties

To understand the underlying reason for the improved electrochemical performance, especially for stable long-term cycling, electrochemical impedance spectroscopy (EIS) experiments for the pristine Fe_2O_3 and the B-containing samples were conducted after different charge/discharge cycles, and the typical Nyquist plots are shown in **Figure 6**. It is observed from Figure 6a that all Nyquist plots have relatively similar shapes, with two semicircles appearing in the high- and middle-frequency regions and a straight line in the low-frequency region. According to the reported model,[28] the smaller semicircle in the high-frequency region represents the impedance of the SEI film (R_{sei}), the larger semicircle in the middle-frequency region is attributed to the charge transfer impedance through the electrode/electrolyte interface (R_{ct}), and the straight line in the low-frequency region corresponds to the impedance of the diffusion of lithium ions in the electrode (the Warburg impedance, W_o) (Figure S6a, Supporting Information). Using a nonlinear least squares fit with the ZView software, the values of R_{sei} and R_{ct} were determined and are summarized in **Table 1**. The B-containing nanocomposites exhibited smaller values of R_{ct} compared with the pristine Fe_2O_3, which indicates that an easier surface reaction process occurred. As observed in Figure 3, the as-prepared B-containing iron oxide nanocomposites exhibited significantly reduced particle size, which enlarges the specific surface area and provides more active reaction sites. In addition, the multiphase structure also possibly provides effective electron conductive paths due to the enriched grain boundary. All these should facilitate reversible redox reactions during the electrochemical processes.

To further investigate the diffusion behavior of Li^+ ion in the electrode materials, the real impedance (Z_{Re}) was replotted against the reciprocal square root of the lower angular frequencies ($\omega^{-1/2}$) in Figure S6b (Supporting Information), and the Warburg impedance coefficient (σ_ω) was derived from the slope of straight line, according to Equation (4)[29]

$$Z_{Re} = R_{et} + R_{sei} + R_{ct} + \sigma_\omega \omega^{-1/2} \tag{4}$$

Then, the diffusion coefficient values of the Li^+ ions (D_{Li}) in the bulk electrode materials can be determined using Equation (5).[30]

$$D_{Li} = \frac{1}{2}\left(\frac{RT}{AF^2C\sigma_\omega}\right)^2 \tag{5}$$

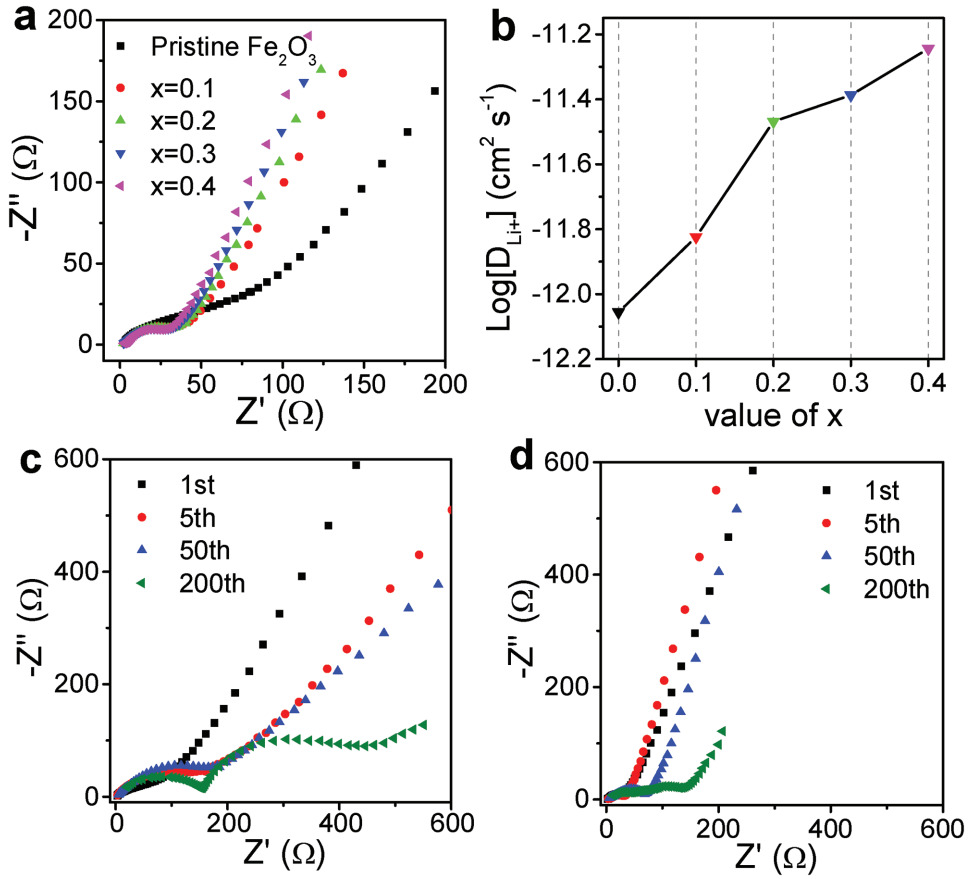

Figure 6. a) Nyquist plots and plot of diffusion coefficient values for Li^+ ions (D_{Li}) of b) pristine Fe_2O_3 and B-containing samples after 1 charge/discharge cycle. Nyquist plots of c) pristine Fe_2O_3 and d) B-containing ($x = 0.2$) samples as a function of cycle.

Table 1. The impedance parameters of the pristine Fe_2O_3 and B-containing samples after first charge/discharge cycle.

Sample	R_{sei} [Ω]	R_{ct} [Ω]	σ_ω [Ω cm^2 s$^{-1/2}$]	D_{Li} [cm^2 s^{-1}]
Fe_2O_3	17.7	18.3	190.6	8.8×10^{-13}
$x = 0.1$	15.3	15.6	143.8	1.5×10^{-12}
$x = 0.2$	10.2	11.6	96.9	3.4×10^{-12}
$x = 0.3$	8.5	11.8	88.2	4.1×10^{-12}
$x = 0.4$	5.8	11.9	74.5	5.7×10^{-12}

where R is the gas constant, T is the absolute temperature, F is Faraday's constant, A is the area of the electrode surface, and C is the molar concentration of Li^+ ions (mol cm^{-3}). The results are also summarized in Table 1 and Figure 6b. The calculated D_{Li} values for the prepared B-containing iron oxide nanocomposites are approximately 1.5×10^{-12} to 5.7×10^{-12} cm^2 s^{-1}, which is an order of magnitude higher than that of the pristine Fe_2O_3 (8.8×10^{-13} cm^2 s^{-1}). Specifically, the diffusivity of Li^+ ions was significantly enhanced after the formation of oxide nanocomposites by reacting with $LiBH_4$. This is possibly related to the reduced particle size and the multiphase structure of the resultant B-containing samples. As described above, the as-prepared samples are identified to be oxide composites mainly composed of Fe_2O_3, Fe_3O_4, $Li_2Fe_3O_5$, and B_2O_3 with ≈10 nm of primary particle sizes. The multiphase structure offers abundant grain boundaries, which can work as diffusion pathways. Moreover, the reduced particle size shortens the diffusion distance of Li^+ ions. Thus, according to the above discussion, the improved electrochemical performance of the prepared B-containing iron oxide nanocomposites can mainly be attributed to their lower charge-transfer resistance values and the higher Li^+ diffusivities caused by their multiphase structure and reduced particle size.

Figure 6c and d illustrate the Nyquist plots of pristine Fe_2O_3 and the B-containing nanocomposite as functions of the cycles. The fitting parameters are summarized in **Table 2**. It is observed that the R_{sei} values of the pristine Fe_2O_3 exhibited a continuous and dramatic increase upon cycling, as they increased 8fold from 17.7 to 142.6 Ω after 200 cycles. Interestingly, the R_{sei} values only increased slightly from 10.2 to 47.8 Ω upon cycling. This indicates that the presence of amorphous B_2O_3 possibly results in the formation of a stable solid-electrolyte interphase (SEI) film on the surface of iron oxides that facilitates the improvement of cycling stability. This conjecture was further confirmed by XPS analysis. As shown in **Figure 7**, the F 1s XPS peak assignable to LiF, an important SEI component in the $LiPF_6$-based electrolyte, remained nearly constant for the prepared B-containing oxide nanocomposite after the initial five cycles. However, it exhibited a tendency of first increase and then decrease for the pristine Fe_2O_3 upon cycling, possibly due to the repeated formation and exfoliation of SEI film caused by the pulverization and fracture of Fe_2O_3 particles.[31] Moreover, the R_{ct} values for both the pristine Fe_2O_3 and the B-containing nanocomposite increased progressively as the number of cycles increased; an additional semicircle in the low-frequency region even appeared after 200 cycles (Figure 6c,d), representing the gradually increasing charge-transfer resistances, possibly due to deteriorated surface states. However, the rate of increase in the R_{ct} value from 11.6 to 86.9 Ω was relatively smaller for the B-containing nanocomposite. This reveals that the B-containing nanocomposite surface remained highly reactive and is responsible for the prolonged cycling life. In addition, it is noteworthy that the D_{Li} value was calculated as 4.9×10^{-11} cm^2 s^{-1} for the B-containing nanocomposite after 200 cycles, which is considerably higher than that of the pristine Fe_2O_3 (3.1×10^{-13} cm^2 s^{-1}). This result suggests that there was still a higher mobility for Li^+ diffusion in the B-containing nanocomposite, even after 200 cycles; this mobility promotes good cycling durability.

Figure 8a–h displays photographs of the cycled wafer electrodes of pristine Fe_2O_3 and the B-containing nanocomposite. For pristine Fe_2O_3, the exposed Cu current collector was clearly observed due to exfoliation of active materials after only 5 cycles, and further active materials were lost upon cycling (Figure 8a–d), which can be attributed to the severe pulverization and fracture (Figure S6c, Supporting Information) caused by a large volume change and poor conductivity upon charging/discharging. This explains the relatively poor cycling stability of the pristine Fe_2O_3, as shown in Figure 4b. Interestingly, the wafer electrode made of the B-containing nanocomposite maintained good integrity even after 200 cycles, and there was nearly negligible loss of active materials (Figure 8e–h). This result was further evidenced by SEM observation, as the electrode surface of the 200-cycled B-containing nanocomposite was still smooth and without observable cracks (Figure S6d, Supporting Information); this appearance represents significantly alleviated pulverization and fracture upon cycling. This can be ascribed to the greatly reduced particle size and the in situ-formed amorphous B_2O_3, as observed in Figure 3. It is generally accepted that reducing particle size effectively increases surface-to-volume ratios, which allows quick relaxation of stress generated during lithiation/delithiation.[32] In addition, the presence of amorphous B_2O_3 facilitates the formation of a stable SEI

Table 2. The impedance parameters of the pristine Fe_2O_3 and the B-containing ($x = 0.2$) sample at different cycles.

Fe_2O_3	R_{sei} [Ω]	R_{ct} [Ω]	σ_ω [Ω cm^2 s$^{-1/2}$]	D_{Li} [cm^2 s^{-1}]	$x = 0.2$	R_{sei} [Ω]	R_{ct} [Ω]	σ_ω [Ω cm^2 s$^{-1/2}$]	D_{Li} [cm^2 s^{-1}]
1st	17.7	18.3	190.6	8.8×10^{-13}	1st	10.2	11.6	96.9	3.4×10^{-12}
10th	30.8	52.4	193.9	8.5×10^{-13}	10th	11.4	14.7	48.7	1.3×10^{-11}
50th	42.4	106.1	267.1	4.4×10^{-13}	50th	18.4	29.1	42.1	1.8×10^{-11}
100th	67.3	134.6	288.8	3.8×10^{-13}	100th	21.6	54.9	29.4	3.6×10^{-11}
200th	142.6	254.6	320.8	3.1×10^{-13}	200th	47.8	86.9	25.6	4.9×10^{-11}

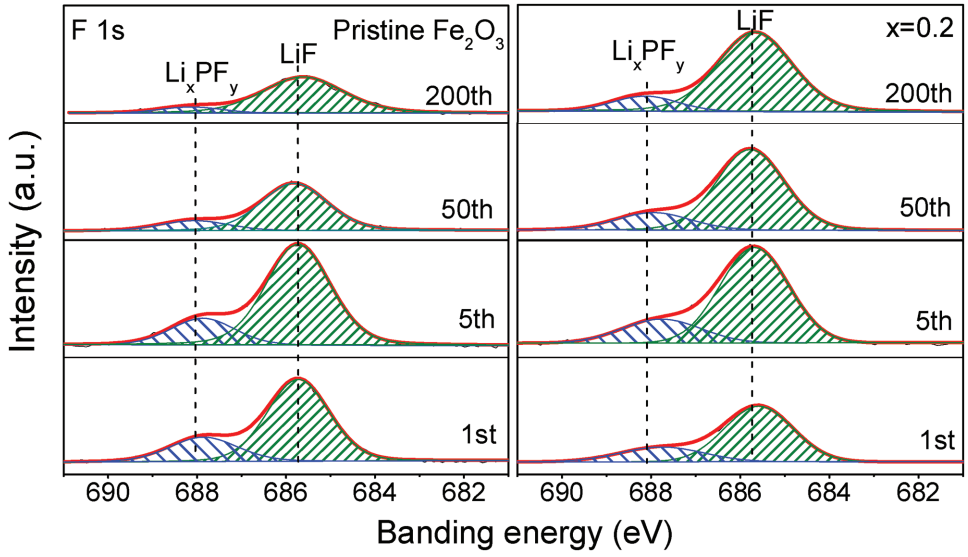

Figure 7. High-resolution XPS spectra of F 1s for pristine Fe_2O_3 and B-containing ($x = 0.2$) electrodes at selected cycles.

layer, as characterized by EIS (Figure 6) and XPS (Figure 7), and may function as a good strain buffer to accommodate volume changes. All these features effectively prevent the pulverization and fracture of the active iron oxide particles upon lithiation/delithiation. As a result, a significantly improved cycling stability was achieved for the prepared B-containing nanocomposites.

To evaluate the general applicability of the strategy developed in this work, further attempts to improve the cycling stability of Fe_2O_3 and NiO anodes were conducted by reacting with $NaBH_4$

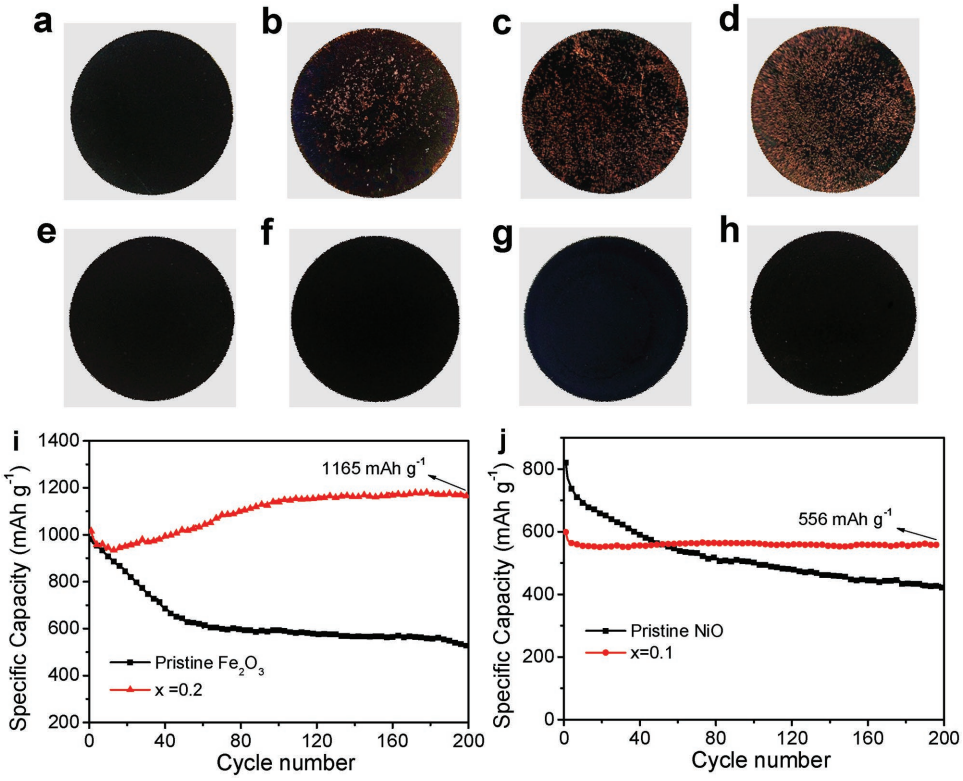

Figure 8. Photographs of cycled wafer electrodes for a–d) pristine Fe_2O_3 and e–h) B-containing ($x = 0.2$) samples: a,e) after 1 cycle, b,f) after 5 cycles, c,g) after 50 cycles, and d,h) after 200 cycles. Cycling performance curves of i) pristine Fe_2O_3 and B-containing samples prepared from Fe_2O_3-$x$$NaBH_4$, j) pristine NiO and B-containing samples prepared from NiO–$x$$LiBH_4$ in the potential range of 0.01–3 V (vs Li/Li^+) at 100 mA g^{-1}.

and $LiBH_4$, respectively. Two samples with compositions of Fe_2O_3–0.2$NaBH_4$ and NiO–0.1$LiBH_4$ were designed and prepared by ball milling at room temperature followed by dynamic heating to 350°C. The prepared samples were subjected to galvanostatic charging/discharging measurements. The results are shown in Figure 8i,j. It was observed that the specific capacity of the prepared Fe_2O_3–0.2$NaBH_4$ sample stabilized at 1165 mAh g^{-1} after 200 cycles when it was cycled at a current density of 100 mA g^{-1} in the potential range of 0.01–3 V (vs Li/Li^+) (Figure 8i), which is largely superior to the pristine Fe_2O_3, for which only 525 mA g^{-1} of capacity remained under these conditions. This indicates that the cycling stability of Fe_2O_3 was remarkably improved by reacting with $NaBH_4$ as an analogue of $LiBH_4$. Moreover, this strategy also succeeded in improving the cycling durability of NiO anode by reacting with $LiBH_4$, as the cycling capacity retention of the prepared NiO-0.1$LiBH_4$ sample was determined to be 93.1% after 200 cycles but only 51.7% for the pristine NiO anode (Figure 8j). More importantly, a full cell assembled using the prepared Fe_2O_3–0.2$LiBH_4$ nanocomposite as anode and home-made $Li_{1.2}Ni_{0.13}Co_{0.13}Mn_{0.54}O_2$ (LNCMO) as cathode, offered good electrochemical energy storage performance when cycled at 0.1 C with the potential widow of 1.0–3.9 V (**Figure 9**). As shown in Figure 9b,c, the initial discharge capacity was determined to be 770 mAh g^{-1} based on anode mass loading with a working potential plateau range of 1.7–3.0 V. After 20 cycles, the reversible capacity remained at 710 mAh g^{-1} with 92% capacity retention, which is superior to previous reports.[33] In addition, two assembled full cells with LNCMO/Fe_2O_3–0.2$LiBH_4$ nanocomposite readily powered an LED array using 22 green LED bulbs with 3 V and a 440 mA rating (Figure 9d). We therefore believe that chemically reacting with metal borohydrides is a viable and general strategy for improving the cycling stability of micro-sized transition metal oxide anodes, which opens a new avenue for developing anode materials with high capacity and long cycle life for practical use in next-generation Li-ion batteries.

3. Conclusion

B-containing iron oxide nanocomposites were successfully prepared by ball milling mixtures of Fe_2O_3–$x$$LiBH_4$ and subsequent heating to 350 °C. During this ball milling and heating, Fe_2O_3 reacted with $LiBH_4$ and was gradually reduced to Fe_3O_4, $Li_2Fe_3O_5$, and even metallic Fe. This was accompanied by the release of hydrogen and the production of B_2O_3. SEM and TEM observation displayed a powdery morphology measuring ≈500 nm and composed of 10 nm nanoparticles. The prepared B-containing nanocomposites exhibited superior electrochemical lithium storage performance, with significantly improved cycling stability and enhanced rate capability. At 100 mA g^{-1}, the sample prepared from Fe_2O_3–0.2$LiBH_4$ delivered initial discharge and charge capacities of 1387 and 1051 mAh g^{-1}, which are higher than those of pristine Fe_2O_3 (1276 and 981 mAh g^{-1}). After 200 cycles, the specific capacity of the sample prepared from Fe_2O_3–0.2$LiBH_4$ remained at 1148 mAh g^{-1}, which is nearly twice that of the pristine Fe_2O_3 after 200 cycles. Even at a high rate of 2000 mA g^{-1}, the specific capacity of the B-containing nanocomposite still reached ≈660 mAh g^{-1}; in contrast, the capacity for pristine Fe_2O_3 under the same conditions was only 210 mAh g^{-1}. EIS analyses revealed that the electrodes made of B-containing nanocomposites exhibited lower charge-transfer resistance values and higher Li^+

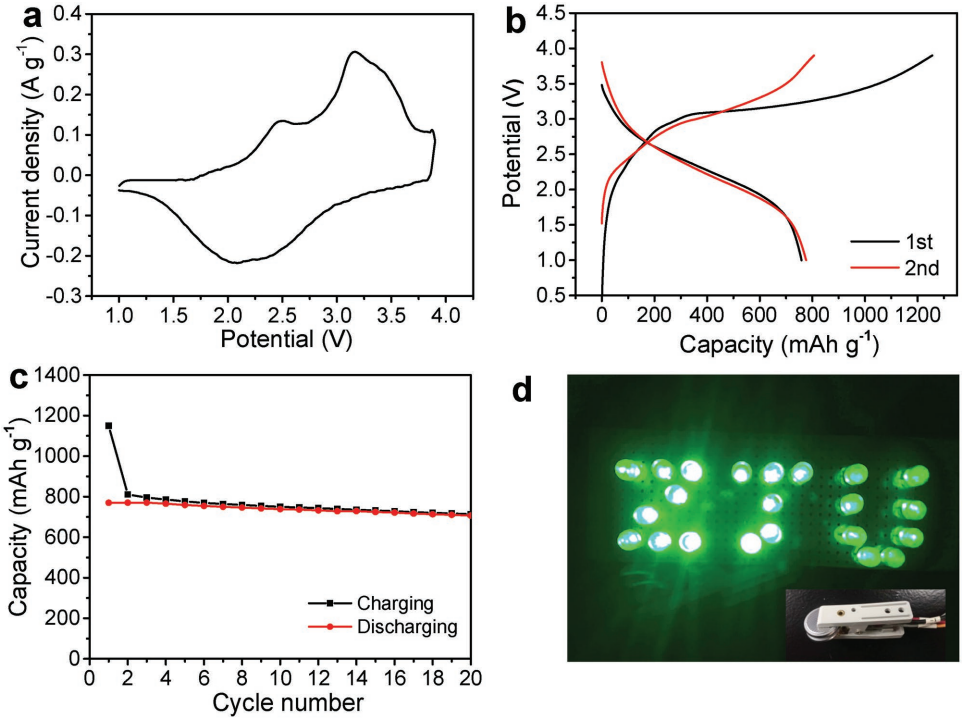

Figure 9. a) CV curve, b) charge–discharge profiles, and c) cycling performance of a LNCMO/Fe_2O_3–0.2$LiBH_4$ nanocomposite full cell, and d) photograph of LED array powered by two LNCMO/Fe_2O_3–0.2$LiBH_4$ nanocomposite full cells.

diffusivities than the electrode made of pristine Fe_2O_3. Further optical and SEM observation showed good integrity without appreciable exfoliation of active materials for the electrode made of B-containing nanocomposite, even after 200 cycles. Contrastingly, the exposed Cu current collector was clearly observed on pristine Fe_2O_3 after only 5 cycles. Therefore, the reduced charge-transfer resistance, increased diffusivity of Li^+ ions and alleviated pulverization and fracture, caused by the remarkably reduced particle size and formation of a stable SEI film, are responsible for the significantly improved electrochemical Li storage properties of the B-containing iron oxide nanocomposites. These results suggest a simple, effective, scalable approach to prepare high-performance oxide anode materials for future LIB applications.

4. Experimental Section

Material Preparation: The starting chemicals, Fe_2O_3 (purity 98%) and $LiBH_4$ (purity 95%), were commercially purchased from Alfa Aesar and used as received. A mixture with compositions of Fe_2O_3–$x$$LiBH_4$ (x = 0, 0.1, 0.2, 0.3, 0.4) was first ball milled on a planetary ball mill (QM-3SP4, Nanjing) at 300 rpm for 2 h under an argon atmosphere. The ball-to-sample weight ratio was approximately 40:1. A gas valve, which can be connected to a pressure gauge for measuring the internal pressure change or a MS for analyzing the composition of gaseous products, was mounted on the cover of the milling jar. After ball milling, the resultant product was transferred to a stainless-steel tube reactor and then gradually heated from ambient temperature to 350 °C at a rate of 2 °C min^{-1} to produce the target materials.

Characterization: The gaseous product was analyzed with a QIC-20 mass spectrometer (Hiden, England). Structural identification was performed on a MiniFlex 600 Rigaku XRD with Cu Kα radiation operating at 40 kV and 15 mA. The XRD data were collected in 0.02° increments between scattering angles of 10° and 90° (2θ) at room temperature, and fitted using the Rietveld method with General Structure Analysis System software. The FTIR spectra were recorded with a Bruker Tensor 27 unit (Germany) in transmission mode. The sample was first mixed with potassium bromide (KBr) in a 1:100 weight ratio and then cold-pressed to form a pellet. XPS analyses were conducted on a Thermo Scientific ESCALAB 250Xi system equipped with an Al Kα (1486.6 eV) X-ray source. The XPS data were calibrated using the adventitious C 1s signal at 284.8 eV as a reference. The binding energy spectra were fitted by XPSPEAK software. The sample morphologies were characterized using a field emission SEM (Hitachi SU70 Japan) and a HRTEM (FEI Tecnai G2 F20, USA, operating at 200 kV). The EDS was employed to analyze the distribution of elemental Fe and O in the samples. For the cycled electrodes, anhydrous diethyl carbonate (DEC) was used to wash away the remaining electrolyte on the surface before SEM examination.

Electrochemical Measurements: The electrochemical properties of the prepared samples, as anode materials, were evaluated by a galvanostatic charge-discharge technique on 2025 coin-type half-cells, which were assembled in an argon-filled glove box (MBRAUN, Germany) with less than 0.1 ppm of oxygen and water content. The working electrode was prepared by coating the slurry consisting of 70 wt% active material, 20 wt% acetylene black as the conductive agent, and 10 wt% sodium alginate as the binder on a 13 mm copper foil and then dried at 120 °C in vacuum for 12 h. The mass loading of the active material was ≈1.5 mg cm^{-2} for each electrode. Pure lithium foil was used as the counter/reference electrode, a solution of 1 M $LiPF_6$ with ethylene carbonate/diethyl carbonate/dimethyl carbonate (EC/DEC/DMC, 1:1:1 by volume) and 1 vol% fluoroethylene carbonate (FEC) was used as the electrolyte, and a Celgard 2400 membrane was used as the separator. The assembled cells were galvanostatically discharged (lithiation)/charged (delithiation) in a potential range of 0.01–3 V (vs Li/Li^+) at a constant current density of 100 mA g^{-1} using a Neware battery testing system (Shenzhen, China) at 26 ± 1 °C. CV measurements were carried out on an Arbin potentiostat (BT-2000, USA) at a scan rate of 0.1 mV s^{-1}. EIS results were recorded with an Ivium Vertex electrochemical workstation (The Netherlands) using a 5 mV amplitude, with a frequency range from 100 kHz to 10 mHz. In a full cell, the prepared Fe_2O_3–0.2$LiBH_4$ nanocomposite was used as anode and home-made LNCMO as cathode. The active material weight ratio of the anode to the cathode was carefully balanced and set at 1:12. 2025 coin type cells were used with 1 M $LiPF_6$ in EC/DEC/DMC (1:1:1 by volume) and 1 vol% FEC as electrolyte, and Celgard 2400 membrane as separator. The fabricated full cell was galvanostatically cycled at 0.1 C within the potential widow of 1.0–3.9 V based on the CV profiles.

Supporting Information

Supporting Information is available from the Wiley Online Library or from the author.

Acknowledgements

Y.C. and Y.X.Y. contributed equally to this work. The authors gratefully acknowledge the financial support from the National Natural Science Foundation of China (51471152, 51571178, and 51621001), the National Materials Genome Project (2016YFB0700600), the Natural Science Foundation of Zhejiang Province (LR16E010002), the Program for Innovative Research Team in University, Ministry of Education of China (IRT13037), and the National Youth Top-Notch Talent Support Program.

Received: January 19, 2017
Revised: February 2, 2017
Published online: March 15, 2017

[1] a) J.-M. Tarascon, M. Armand, *Nature* **2001**, *414*, 359; b) J. B. Goodenough, Y. Kim, *Chem. Mater.* **2010**, *55*, 587; c) M. Armand, J.-M. Tarascon, *Nature* **2008**, *451*, 652; d) L. Suo, O. Borodin, T. Gao, M. Olguin, J. Ho, X. Fan, C. Luo, C. Wang, K. Xu, *Science* **2015**, *350*, 938; e) D. Deng, *Energy Sci. Eng.* **2015**, *3*, 385.

[2] a) Y. Idota, T. Kubota, A. Matsufuji, Y. Maekawa, T. Miyasaka, *Science* **1997**, *276*, 1395; b) Y. Oumellal, A. Rougier, G. A. Nazri, J.-M. Tarascon, L. Aymard, *Nat. Mater.* **2008**, *7*, 916; c) A. Magasinski, P. Dixon, B. Hertzberg, A. Kvit, J. Ayala, G. Yushin, *Nat. Mater.* **2010**, *9*, 353; d) N. Liu, Z. D. Lu, J. Zhao, M. T. McDowell, H. W. Lee, W. T. Zhao, Y. Cui, *Nat. Nanotechnol.* **2014**, *9*, 187; e) N. Nitta, F. Wu, J. T. Lee, G. Yushin, *Mater. Todays* **2015**, *18*, 252; f) V. Aravindan, Y. S. Lee, S. Madavi, *Adv. Energy Mater.* **2015**, *5*, 140225; g) J. Xie, Q. C. Zhang, *J. Mater. Chem. A* **2016**, *4*, 2091.

[3] a) P. Poizot, S. Laruelle, S. Grugeon, L. Dupont, J.-M. Tarascon, *Nature* **2000**, *407*, 496; b) J. Chen, F. Y. Cheng, *Acc. Chem. Res.* **2009**, *42*, 713; c) C. Liang, M. X. Gao, H. G. Pan, Y. F. Liu, M. Yan, *J. Alloys Compd.* **2013**, *575*, 246; d) Z. Y. Wang, L. Zhou, X. W. Lou, *Adv. Mater.* **2012**, *24*, 1903; e) C. M. Ban, Z. C. Wu, D. T. Gillaspie, L. Chen, Y. F. Yan, J. L. Blackburn, A. C. Dillon, *Adv. Mater.* **2010**, *22*, E145; f) W. W. Zhou, C. W. Cheng, J. P. Liu, Y. Y. Tay, J. Jiang, X. T. Jia, J. X. Zhang, H. Gong, H. H. Hng, T. Yu, H. J. Fan, *Adv. Funct. Mater.* **2011**, *21*, 2439; g) S. H. Yu, S. H. Lee, D. J. Lee, Y. E. Sung, T. Hyeon, *Small* **2016**, *12*, 2146; h) Y. X. Zeng, M. H. Yu, Y. Meng, P. P. Fang, X. H. Lu, Y. X. Tong, *Adv. Energy Mater.* **2016**, *6*, 1601053.

[4] J. Li, H. M. Dahn, R. J. Sanderson, A. D. W. Todd, J. R. Dahn, *J. Electrochem. Soc.* **2008**, *155*, A975.

[5] a) S. W. Cao, Y. J. Zhu, *J. Phys. Chem. C* **2008**, *112*, 6253; b) H. J. Kim, K. I. Choi, A. Q. Pan, I. D. Kim, H. R. Kim, K. M. Kim, C. W. Na, G. Z. Cao, J. H. Lee, *J. Mater. Chem.* **2011**, *21*, 6549; c) E. Kang, Y. S. Jung, A. S. Cavanagh, G. H. Kim, S. M. George, A. C. Dillon, J. K. Kim, J. Lee, *Adv. Funct. Mater.* **2011**, *21*, 2430; d) J. Su, M. H. Cao, L. Ren, C. W. Hu, *J. Phys. Chem. C* **2011**, *115*, 14469; e) Y. H. Xu, G. Q. Jian, Y. H. Liu, Y. J. Zhu, M. R. Zachariah, C. S. Wang, *Nano Energy* **2014**, *3*, 26.

[6] X. H. Chai, C. S. Shi, E. Z. Liu, J. J. Li, N. Q. Zhao, C. N. He, *Appl. Surf. Sci.* **2015**, *347*, 178.

[7] a) L. M. Bronstein, X. Huang, J. Retrum, A. Schmucker, M. Pink, B. D. Stein, B. Dragnea, *Chem. Mater.* **2007**, *19*, 3624; b) W. Cho, S. Park, M. Oh, *Chem. Commun.* **2011**, *47*, 4138; c) J. Chen, L. N. Xu, W. Y. Li, X. L. Gou, *Adv. Mater.* **2005**, *17*, 582; d) M. V. Reddy, T. Yu, C. H. Sow, Z. X. Shen, C. T. Lim, G. V. S. Rao, B. V. R. Chowdari, *Adv. Funct. Mater.* **2007**, *17*, 2792; e) S. Y. Zeng, K. B. Tang, T. W. Li, Z. H. Liang, D. Wang, Y. K. Wang, W. W. Zhou, *J. Phys. Chem. C* **2007**, *111*, 10217; f) K. Z. Cao, L. F. Jiao, H. Q. Liu, Y. C. Liu, Y. J. Wang, Z. P. Guo, H. T. Yuan, *Adv. Energy Mater.* **2015**, *5*, 1401; g) X. Gu, L. Chen, Z. C. Ju, H. Y. Xu, J. Yang, Y. T. Qian, *Adv. Funct. Mater.* **2013**, *23*, 4049; h) C. J. Niu, J. S. Meng, X. P. Wang, C. H. Han, M. Y. Yan, K. N. Zhao, X. M. Xu, W. H. Ren, Y. L. Zhao, L. Xu, Q. J. Zhang, D. Y. Zhao, L. Q. Mai, *Nat. Commun.* **2015**, *6*, 7402; i) Y. X. Wang, J. P. Yang, S. L. Chou, H. K. Liu, W. X. Zhang, D. Y. Zhao, S. X. Dou, *Nat. Commun.* **2015**, *6*, 8689.

[8] Y. M. Lin, P. R. Abel, A. Heller, C. B. Mullins, *J. Phys. Chem. Lett.* **2011**, *2*, 2885.

[9] L. Chen, H. Y. Xu, L. Li, F. F. Wu, J. Yang, Y. T. Qian, *J. Power Sources* **2014**, *245*, 429.

[10] D. N. Lei, M. Zhang, B. H. Qu, L. B. Chen, Y. G. Wang, E. D. Zhang, Z. Xu, Q. H. Li, T. H. Wang, *Nanoscale* **2012**, *4*, 3422.

[11] L. Zhang, H. B. Wu, R. Xu, X. W. Lou, *CrystEngComm* **2013**, *15*, 9332.

[12] B. Wang, J. S. Chen, H. B. Wu, Z. Y. Wang, X. W. Lou, *J. Am. Chem. Soc.* **2011**, *133*, 17146.

[13] a) L. Zhang, H. B. Wu, X. W. Lou, *Adv. Energy Mater.* **2014**, *4*, 1300958; b) E. Kang, Y. S. Jung, G. H. Kim, J. Chun, U. Wiesner, A. C. Dillon, J. K. Kim, J. Lee, *Adv. Funct. Mater.* **2011**, *21*, 4349; c) C. L. Liang, T. Zhai, W. Wang, J. Chen, W. X. Zhao, X. H. Lu, Y. X. Tong, *J. Mater. Chem. A* **2014**, *2*, 7214.

[14] Z. Y. Wang, D. Y. Luan, S. Madhavi, Y. Hu, X. W. Lou, *Energy Environ. Sci.* **2012**, *5*, 5252.

[15] Q. Zhou, Z. B. Zhao, Z. Y. Wang, Y. F. Dong, X. Z. Wang, Y. Gogotsi, J. S. Qiu, *Nanoscale* **2014**, *6*, 2286.

[16] Q. Y. An, F. Lv, Q. Q. Liu, C. H. Han, K. N. Zhao, J. Z. Sheng, Q. L. Wei, M. Y. Yan, L. Q. Mai, *Nano Lett.* **2014**, *14*, 6250.

[17] Y. Huang, Z. X. Lin, M. B. Zheng, T. H. Wang, J. Z. Yang, F. S. Yuan, X. Y. Lu, L. Liu, D. P. Sun, *J. Power Sources* **2016**, *307*, 649.

[18] D. Z. Kong, C. W. Cheng, Y. Wang, B. Liu, Z. X. Huang, H. Y. Yang, *J. Mater. Chem. A* **2016**, *30*, 11800.

[19] a) M. Matsuo, Y. Nakamori, S. Orimo, H. Maekawa, H. Takamura, *Appl. Phys. Lett.* **2007**, *91*, 224103; b) M. Matsuo, A. Orimo, *Adv. Energy Mater.* **2011**, *1*, 161; c) A. Unemoto, M. Matsuo, S. Orimo, *Adv. Funct. Mater.* **2014**, *24*, 2267; d) R. Mohtadi, A. Remhof, P. Jena, *J. Phys.: Condens. Matter* **2016**, *28*, 353001.

[20] Y. Hori, T. Ida, M. Mizuno, *Comput. Theor. Chem.* **2016**, *1076*, 86.

[21] a) B. N. Rao, P. R. Kumar, O. Padmaraj, M. Venkateswarlu, N. Satyanarayana, *RSC Adv.* **2015**, *5*, 34761; b) B. Jin, G. Y. Chen, X. B. Zhong, Y. Liu, K. Y. Zhou, P. Sun, P. Lu, W. X. Zhang, J. C. Liang, *Ceram. Int.* **2014**, *40*, 10359.

[22] X. D. Wu, Z. X. Wang, L. Q. Chen, X. J. Huang, *Solid State Ion* **2004**, *170*, 117.

[23] a) G. F. Xia, N. Li, D. Y. Li, D. Y. Li, R. Q. Liu, N. Xiao, D. Tian, *Mater. Lett.* **2012**, *79*, 58; b) K. P. C. Yao, D. G. Kwabi, R. A. Quinlan, A. N. Mansour, A. Grimaud, Y. L. Lee, Y. C. Lu, Y. Shao-Horn, *J. Electrochem. Soc.* **2013**, *160*, A824.

[24] K. Kaneko, *J. Met. Finish. Soc. Jpn.* **1986**, *37*, 46.

[25] F. C. Zheng, M. N. He, Y. Yang, Q. W. Chen, *Nanoscale* **2015**, *7*, 3410.

[26] S. M. Xu, C. M. Hessel, H. Ren, R. B. Yu, Q. Jin, M. Yang, H. J. Zhao, D. Wang, *Energy Environ. Sci.* **2014**, *7*, 632.

[27] J. Morales, L. Sanchez, F. Martin, F. Berry, X. L. Ren, *J. Electrochem. Soc.* **2005**, *152*, A1748.

[28] J. C. Guo, A. Sun, X. L. Chen, C. S. Wang, A. Manivannan, *Electrochim. Acta* **2011**, *56*, 3981.

[29] A. J. Brad, L. R. Faulkner, *Electrochemical Methods: Fundamentals and Applications*, Wiley, New York, USA **2001**.

[30] N. Ding, J. Xu, Y. X. Yao, G. Wegner, X. Fang, C. H. Chen, I. Lieberwirth, *Solid State Ion* **2009**, *180*, 222.

[31] W. J. Yu, P. X. Hou, F. Li, C. Liu, *J. Mater. Chem.* **2012**, *22*, 13756.

[32] a) J. R. Szczech, J. Song, *Energy Environ. Sci.* **2011**, *4*, 56; b) Y. Zhao, X. F. Li, B. Y, D. B. Xiong, D. J. Li, S. Lawes, X. L. Sun, *Adv. Energy Mater.* **2016**, *6*, 1502175; c) B. L. Ellis, P. Knauth, T. Djenizian, *Adv. Mater.* **2014**, *26*, 3368.

[33] a) L. W. Ji, Z. K. Tan, T. R. Kuykendall, S. Aloni, S. D. Xun, E. Lin, V. Battaglia, Y. G. Zhang, *Phys. Chem. Chem. Phys.* **2011**, *13*, 7170; b) W. H. Xie, L. L. Gu, X. L. Sun, M. T. Liu, S. Y. Li, Q. Wang, D. Q. Liu, D. Y. He, *Electrochim. Acta* **2016**, *220*, 107.

